Thin-Rib and High Aspect Ratio Non-Stochastic Scaffolds by Vacuum Assisted Investment Casting

Vitor H. Carneiro [1],*, Hélder Puga [2] ⓘ**, Nuno Peixinho [1] and José Meireles [1]**

[1] MEtRiCS—Mechanical Engineering and Resource Sustainability Center, Campus of Azurém,
    4800-058 Guimarães, Portugal; peixinho@dem.uminho.pt (N.P.); meireles@dem.uminho.pt (J.M.)
[2] CMEMS—UMinho, University of Minho, Campus of Azurém, 4800-058 Guimarães, Portugal;
    puga@dem.uminho.pt
* Correspondence: d6705@dem.uminho.pt; Tel.: +351-253-510-220

Abstract: Cellular structures are a classic route to obtain high values of specific mechanical properties. This characteristic is advantageous in many fields, from diverse areas such as packaging, transportation industry, and/or medical implants. Recent studies have employed additive manufacturing and casting techniques to obtain non-stochastic cellular materials, thus, generating an in situ control on the overall mechanical properties. Both techniques display issues, such as lack of control at a microstructural level in the additive manufacturing of metallic alloys and the difficulty in casting thin-rib cellular materials (e.g., metallic scaffolds). To mitigate these problems, this study shows a combination of additive manufacturing and investment casting, in which vacuum is used to assist the filling of thin-rib and high aspect-ratio scaffolds. The process uses 3D printing to produce the investment model. Even though, vacuum is fundamental to allow a complete filling of the models, the temperatures of both mold and casting are important to the success of this route. Minimum temperatures of 250 °C for the mold and 700 °C for the casting must be used to guarantee a successful casting. Cast samples shown small deviations relatively to the initial CAD model, mainly small expansions in rib length and contraction in rib thickness may be observed. However, these changes may be advantageous to obtain higher values of aspect ratio in the final samples.

Keywords: scaffold; investment casting; thin-wall; aluminum alloy; vacuum; filling

1. Introduction

Cellular structures, in the form of composite materials, are a classic route to obtain high values of static and dynamic specific mechanical properties [1,2]. This characteristic has always been advantageous in many fields and applications, from diverse areas such as packaging, the transportation industry (e.g., railway [3–5] and aeronautic [6–8]), and medical implants [9–11]. This class of materials, when using a metallic matrix, are classically manufactured by foam blowing agents/gas injection [12–17] and casting with space holders with leachable [18–22] or non-leachable [23–25] particles. Other techniques may also be found by the use of powder metallurgy [26,27] or wire weaving [28–30]. These techniques are able to be produced in an array of specific densities in both open-cell [26,28,31,32] and closed-cell [15,33,34] configurations, both being commonly of stochastic nature.

Recent studies have explored the use of additive manufacturing (e.g., selective metal laser or electron beam melting) [35–39] and metal casting [40,41] to produce non-stochastic cellular materials. This has the advantage of allowing in situ geometric and dimensional control, thus, they are able to display tailored properties [42]. However, the referred processes are known to have inherent problems being; the difficult microstructural control in additively manufactured metals [43–45] and the casting of thin-rib cellular materials. Even though there have been reported casting products with extremely

thin sections (~0.1 mm) and high aspect ratios [46], their application in a metallic scaffold shape is still a challenge. Vacuum assisted high pressure die [47–49] and low pressure casting [50,51] are able to produce thin-walled and/or high detailed structures, however, they are not suited for the manufacturing of intricate three-dimensional complex geometries.

The present study shows a combination of additive manufacturing, in which fused filament fabrication (PLA) is used to produce the intermediate investment model to be cast in ceramic block by investment casting. Although there are already studies that use similar techniques (e.g., 3D printing of sand molds [52–56], wax, and PLA/ABS [52–56]), the proposed study recurs to vacuum as an auxiliary technique for the filling of thin-rib and high aspect ratio complex three-dimensional metallic scaffolds. Additionally, vacuum is also used to promote the sanity of the resultant samples, as it is known to reduce oxide inclusion [57,58] and porosity [59,60].

2. Methodology

2.1. Scaffold Design and Selection

Samples were designed using a basic three-dimensional honeycomb unitary cell configuration, in which the cells are assembled in a matrix (9 by 9 by 8) configuration, according to Figure 1. To generate different casting conditions while keeping the casting volume approximately constant (i.e., amount of material), the linear dimensions of the cells [1] were kept constant changing only the rib angle (Table 1). Figure 1 shown the influence of rib angle in the overall scaffold configuration, where the negative angles (Figure 1a,b) are gradually widened to null angles (cubic cell—Figure 1c) and positive angles (Figure 1d,e) samples. An overall theoretical aspect ratio of 6.7 is maintained across the models due to the square cross section of the ribs.

Table 1. Fundamental unitary cell dimensions.

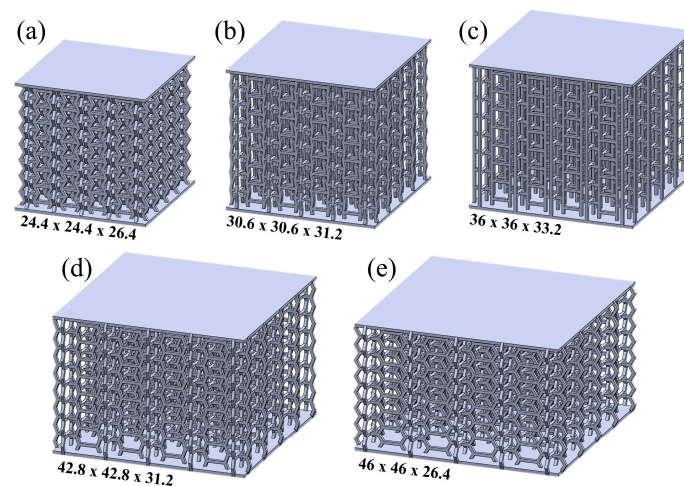| Horizontal Rib Length [mm]	Vertical Rib Length [mm]	Rib Thickness [mm]	Rib Angle [°]	Aspect Ratio (Length/Thickness)
4	2	0.6	−30 to 30	6.7

Figure 1. CAD models for scaffold models (dimensions in mm), with rib angles: (**a**) −30°; (**b**) −20°; (**c**) 0°; (**d**) 20° and (**e**) 30°.

Considering the analysis of mold and casting temperatures in the successful filling of the scaffolds obtained by vacuum assisted investment casting, the CAD models were compared to determine the most difficult sample to manufacture. It is known that in casting procedures, variables such as filling length and distance to the mold wall have a fundamental importance in the overall success of the casting procedure. Thus, the samples were characterized in terms of their diagonal cross-sectional area

(Figure 2a). According to Figure 2, it may be observed that the sample with higher cross section area (consequently higher values of filling length and lower mold wall distance) is the one with a 20° rib angle (Figure 2b). Thus, this was the sample that was selected for this study (Figure 1d).
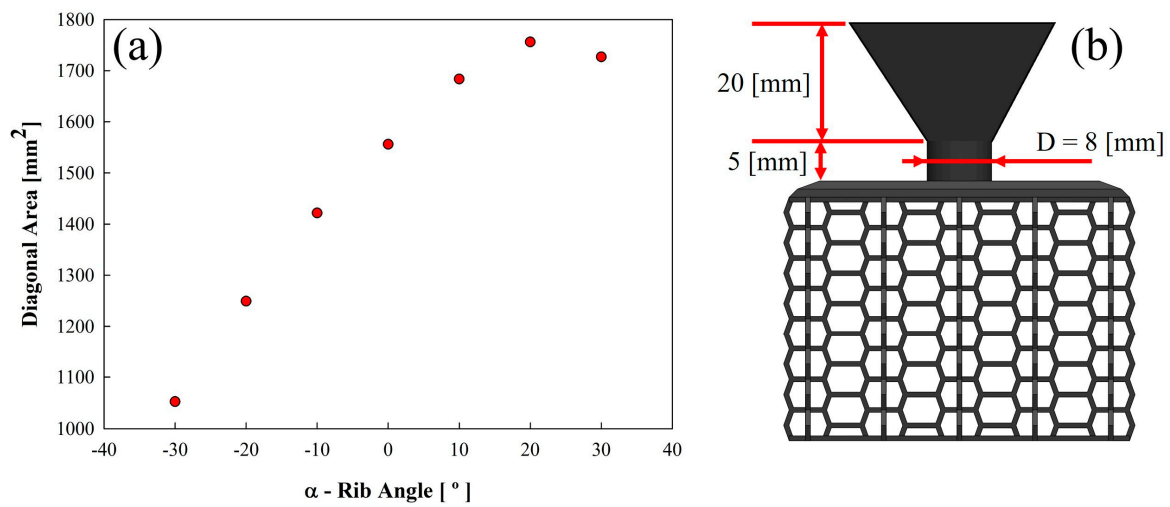

Figure 2. (**a**) Model selection by diagonal area analysis and (**b**) gating and selected model detail.

2.2. Ceramic Block Manufacturing

Molds were manufactured using plaster (GoldStar Omega+, Staffordshire, UK) to produce a ceramic block. According to the manufacturer guidelines, the plaster was subjected to the thermal cycle showed in Figure 3a. Given that 3D printing is used to produce a PLA investment model it may be observed that, according to the thermogravimetric analysis displayed in Figure 3b, the maximum temperature of 730 °C is able to completely eliminate the PLA model and generate the cavity to be filled in the casting process.
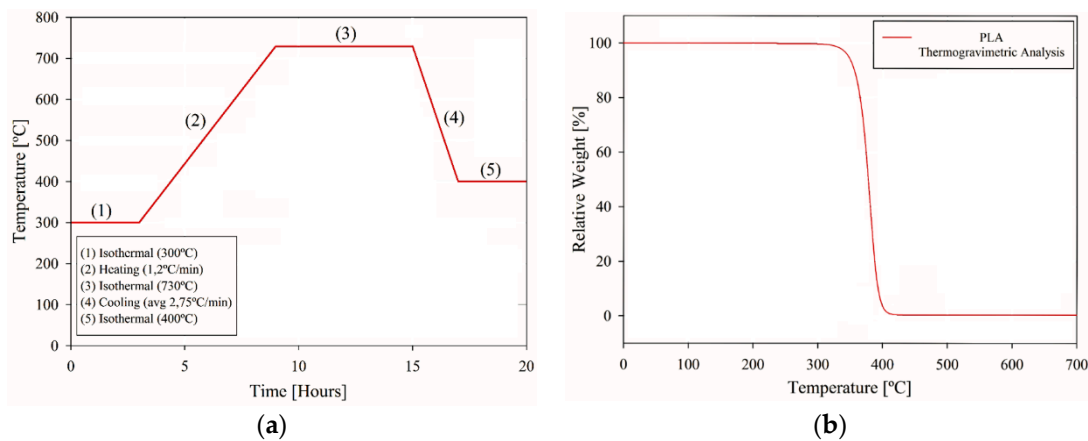

Figure 3. Ceramic block manufacturing: (**a**) mold thermal cycle; (**b**) PLA thermogravimetric analysis.

2.3. Vacuum Assisted Investment Casting

Molds were introduced into an Indutherm MC15+ casting furnace, while 24 (±0.02) g of A356 alloy, 0.05 g (±0.01) of Al_5Ti_1B grain refiner and 0.07 g (±0.01) of $Al_{10}Sr$ eutectic Si modifier are placed in a graphite crucible. After the furnace is closed, the metal composition is heated recurring to induction current to the desired casting temperature. Given the low amount of material to be melted, generally, a complete melting can take up to 1.5 min. After such period the melt is subjected to the induction current to allow a homogenous spreading of the grain refiner and eutectic Si modifier for 3 min. Finally, the melt is cast into the mold where the sample is allowed to solidify for 10 min before tossing the

mold in mild water to remove the plaster. Additionally, to promote a successful filling, vacuum was applied to some sample during the melting and casting procedures.

Table 2 displays the array of mold (T_M) and casting (T_C) temperatures that were studied. For each temperature combination a total of eight samples were produced, in which four where manufactured without vacuum and the remaining samples used vacuum assisted casting.

Table 2. Experimental casting setup.

Mold Temperatures T_M [°C]	Casting Temperatures T_C [°C]	Vacuum Pressure (If Used) [bar]
100 to 400 (50 °C steps)	680 to 740 (10 °C steps)	−1

3. Results

3.1. Influence of Mold and Casting Temperatures

Distinct mold and casting temperatures were used to determine their influence in a successful casting of thin-rib aluminum scaffolds in the presence or absence of auxiliary vacuum. A combination of the referred variables was used, generating the conclusion that their control is fundamental to guarantee a successful casting of the proposed cellular structure. Figure 4 shows a successful attempt to cast the proposed scaffold (20° rib angle, Figure 1d) using vacuum assistance and mold/casting temperatures of, respectively, 250 °C and 700 °C.
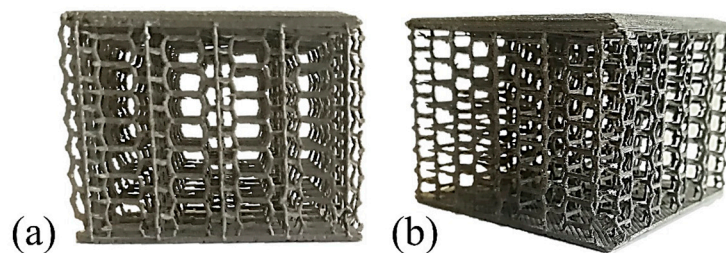

(a)　　　　　　　　(b)

Figure 4. Developed manufacturing process as-cast sample (T_M = 250 °C and T_C = 700 °C, using vacuum assistance): (**a**) front and (**b**) corner views.

Figure 4 shows that the adopted method is able to display a good shape and detail correlation to the CAD model that is displayed in Figure 1d. The unitary cells assume a full three-dimensional honeycomb configuration and are fully connected between themselves, presenting a complete assembly of the scaffold.

It is shown that the use of the described technique, it is possible to reproduce the intended design, however as shown in Figure 5, the use of different temperature has a fundamental role in the obtaining of a successful casting. According to the results presented in Figure 5a, the use of T_M = 200 °C and T_C = 680 °C with vacuum assistance, is not able to guarantee the successful filling of the model. Further increasing the casting temperature by 20 °C (T_M = 200 °C and T_C = 700 °C—Figure 5b), it may be stated that the overall filling is increased, however, it has still shown an absence of material in the sample corners. By the increase of mold temperature (T_M = 250 °C and T_C = 700 °C—Figure 5c) it is possible to guarantee a successful filling of the adopted model, considering that the overall casting process is correctly performed.
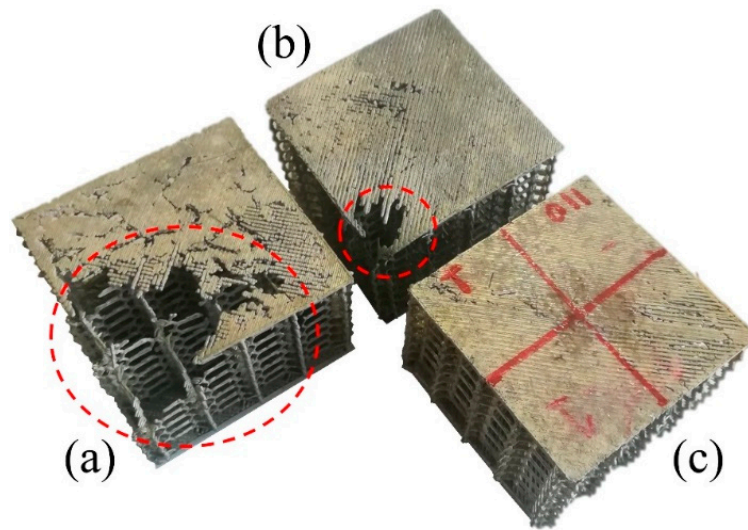
Figure 5. Characterization of average filling using different temperatures using vacuum assistance: (**a**) 83% (±6.3%)—T_M = 200 °C and T_C = 680 °C; (**b**) 92% (±4.1%)—T_M = 200 °C and T_C = 700 °C; and (**c**) complete filling—T_M = 250 °C and T_C = 700 °C.

Overall, it may be determined by the results in Figure 5 that in near complete filling conditions, the increase of mold and casting temperatures is able to enhance the filling by, respectively, 0.16% °C^{-1} and 0.75% °C^{-1}. Thus, it is suggested that the influence of casting temperature is more prominent for the filling of complex aluminum thin-ribs in near complete casting conditions.

These suggestions are further supported by the overall comparison of average sample filling showed in Figure 6. As expected, high temperatures of both mold and casting are extremely useful to allow a complete filling of the model (Figure 5a). However, it is also shown that in the absence of vacuum (Figure 5b), it is not possible to cast the scaffolding structures. Even though, the use of high mold and casting temperatures is able to enhance the filling of gravity casting samples, overall the experimental results suggest a maximum filling of approximately 20%. It could be argued that further increasing the mold and casting temperatures could increase the filling and eventually allow a complete casting in non-vacuum conditions. However, it is also known that the superheating of aluminum alloy melts is extremely hazardous for the final casting products by the decrease in microstructural sanity [61,62]. Thus, minimal mold and casting temperatures should be used, as long as the casting process is not compromised.
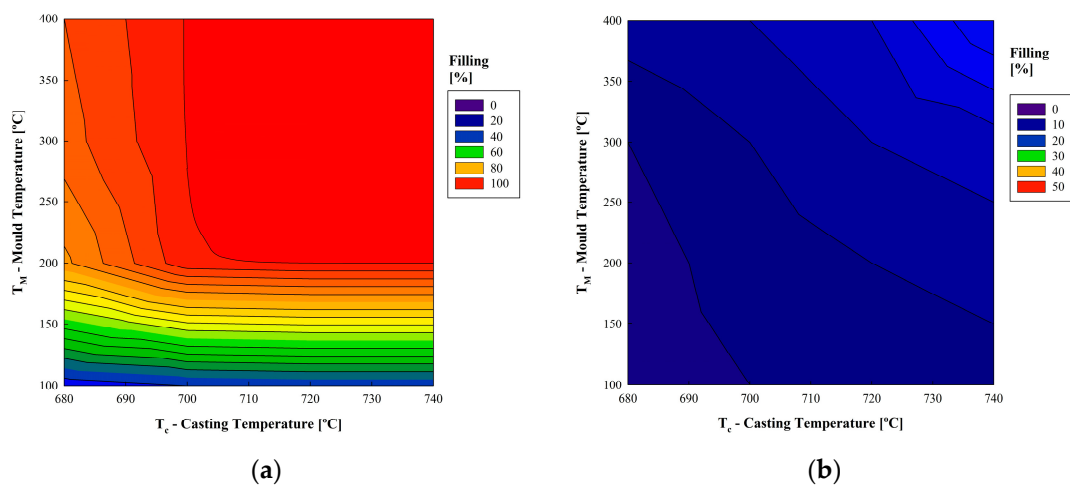

Figure 6. Average sample filling using different combinations of mold and casting temperatures: (**a**) with vacuum; and (**b**) without vacuum.

Considering these facts and observing Figure 5a, it may be stated that the most beneficial combination of mold and casting temperatures for the adopted vacuum assisted investment casting process are, respectively, $T_M = 250\ ^\circ C$ and $T_C = 700\ ^\circ C$. Additionally, it is known that the use of vacuum is beneficial for the overall sanity of aluminum cast products. Reducing the referred temperatures is not recommended given that the thin-rib configuration is easily clogged by the premature alloy solidification due to the high cooling rates in low temperature molds or near solidus configuration in low temperature castings.

3.2. Dimensional Characterization of the Manufacturing Process

The use of investment casting is generally associated with the intent to manufacture samples with a low dimensional deviations, high tolerance, and an elevated replication rate of the investment model [63]. Thus, the adopted process is intended to have the capability of fully reproducing the proposed CAD model (Figure 1d). Figure 7 shows a dimensional analysis of the manufactured samples when compared with the proposed CAD model. It may be observed that, on average the rib length tends to be increased, while it is decreased in terms of thickness.
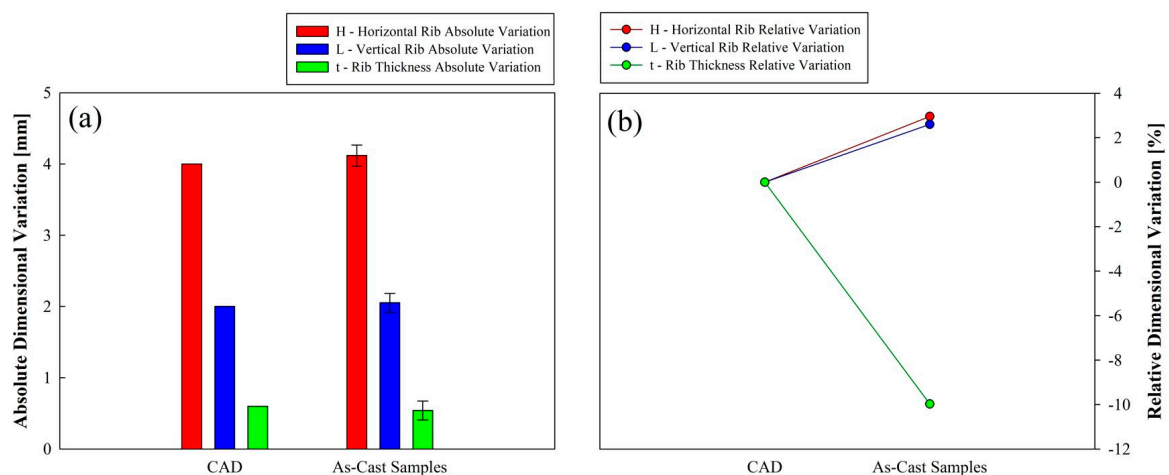

Figure 7. Sample (**a**) absolute and (**b**) relative dimensional variations after casting.

It is known that during its thermal cycle, the plaster releases its water content losing mass, however, the overall mold can suffer an expansion due to the α- to β- transitions in the cristobalite (5.7% in volume) and quartz (4.3% in volume) components of the plaster [64]. Additionally, aluminum alloys suffer from considerable shrinkage and linear contraction during solidification [65,66]. These effects are able to influence the final cast sample dimensions, in which the higher dimensions of rib length show a similar increase in both horizontal and vertical configurations (2.5% expansion—according to Figure 7). The rib thickness shows a more prominent relative variation possessing a near 10% linear contraction. However, when adopting an absolute dimensional variation, these changes may be rendered as negligible: on average, rib length maximum increase is 0.12 mm, while it is reduced by 0.06 mm in thickness. It is also shown that, according to the values of standard deviation, the overall aspect ratio may assume values between 6.1 and 9.8. This implies that the overall dimension change may be beneficial and further increase the aspect ratio.

4. Conclusions

A manufacturing route is presented for the production of thin-rib and high aspect ratio aluminum scaffolds that are modeled as an assembly of three-dimensional honeycomb unitary cells. It is shown that a combination different mold and casting temperatures must be employed to ensure a complete filling of the samples.

A minimum temperature combination of 250 °C for the mold and 700 °C for the casting must be used to guarantee the complete filling of the samples. It is suggested that in near complete casting conditions, the most important factor is the casting temperature. Additionally, it is shown that the vacuum assistance is needed to ensure the success of the procedure.

In terms of dimensional characterization, due to the volumetric changes by the expansion of plaster during its thermal cycle and alloy shrinkage/linear contraction during solidification, the cast specimens tend to increase their rib length and reduce the rib thickness when compared to the CAD model. However, this combination is able to contribute to enhance the overall high aspect ratio and thin-rib configuration that is proposed for the presented manufacturing method.

Author Contributions: Conceptualization, V.H.C. and H.P.; methodology, V.H.C. and H.P.; validation, H.P., N.P. and J.M.; formal analysis, V.H.C. and H.P.; resources, H.P.; data curation, V.H.C., N.P. and J.M.; writing—original draft preparation, V.H.C. and H.P.

Conflicts of Interest: The authors declare no conflict of interest.

References

1. Gibson, L.J.; Ashby, M.F. *Cellular Solids: Structure and Properties*; Cambridge University Press: Cambridge, UK, 1999; ISBN 1-316-02542-X.
2. Ashby, M.F.; Evans, T.; Fleck, N.A.; Hutchinson, J.; Wadley, H.; Gibson, L. *Metal Foams: A Design Guide*; Elsevier: Amsterdam, The Netherlands, 2000; ISBN 0-08-051146-5.
3. Satyal, S.R.; Leshchinsky, B.; Han, J.; Neupane, M. Use of cellular confinement for improved railway performance on soft subgrades. *Geotext. Geomembr.* **2018**, *46*, 190–205. [CrossRef]
4. Sol-Sánchez, M.; Moreno-Navarro, F.; Rubio-Gámez, M.C. The use of elastic elements in railway tracks: A state of the art review. *Constr. Build. Mater.* **2015**, *75*, 293–305. [CrossRef]
5. Xie, S.; Zhou, H. Impact characteristics of a composite energy absorbing bearing structure for railway vehicles. *Compos. Part B Eng.* **2014**, *67*, 455–463. [CrossRef]
6. Le Barbenchon, L.; Girardot, J.; Kopp, J.-B.; Viot, P. Multi-scale foam: 3D structure/compressive behaviour relationship of agglomerated cork. *Materialia* **2019**, *5*, 100219. [CrossRef]
7. Xing, Y.; Yang, X.; Yang, J.; Sun, Y. A theoretical model of honeycomb material arresting system for aircrafts. *Appl. Math. Model.* **2017**, *48*, 316–337. [CrossRef]
8. Yang, X.; Zhang, Z.; Xing, Y.; Yang, J.; Sun, Y. A new theoretical model of aircraft arresting system based on polymeric foam material. *Aerosp. Sci. Technol.* **2017**, *66*, 284–293. [CrossRef]
9. Yan, Q.; Dong, H.; Su, J.; Han, J.; Song, B.; Wei, Q.; Shi, Y. A Review of 3D Printing Technology for Medical Applications. *Engineering* **2018**, *4*, 729–742. [CrossRef]
10. Murr, L.E. Strategies for creating living, additively manufactured, open-cellular metal and alloy implants by promoting osseointegration, osteoinduction and vascularization: An overview. *Recent Adv. Addit. Manuf. Met. Alloys* **2019**, *35*, 231–241. [CrossRef]
11. Carneiro, V.H.; Puga, H. Deformation behaviour of self-expanding magnesium stents based on auxetic chiral lattices. *Ciênc. Tecnol. Mater.* **2016**, *28*, 14–18. [CrossRef]
12. Yang, D.-H.; Hur, B.-Y.; Yang, S.-R. Study on fabrication and foaming mechanism of Mg foam using $CaCO_3$ as blowing agent. *J. Alloys Compd.* **2008**, *461*, 221–227. [CrossRef]
13. Gnyloskurenko, S.V.; Koizumi, T.; Kita, K.; Nakamura, T. Aluminum Metallic Foams Made by Carbonate Foaming Agents. *Resour. Process.* **2013**, *60*, 5–12. [CrossRef]
14. Li, P.; Nguyen, N.V.; Hao, H. Dynamic compressive behaviour of Mg foams manufactured by the direct foaming process. *Mater. Des.* **2016**, *89*, 636–641. [CrossRef]
15. Wang, N.; Maire, E.; Chen, X.; Adrien, J.; Li, Y.; Amani, Y.; Hu, L.; Cheng, Y. Compressive performance and deformation mechanism of the dynamic gas injection aluminum foams. *Mater. Charact.* **2019**, *147*, 11–20. [CrossRef]

16. Heim, K.; García-Moreno, F.; Banhart, J. Particle size and fraction required to stabilise aluminium alloy foams created by gas injection. *Scr. Mater.* **2018**, *153*, 54–58. [CrossRef]

17. Rajak, D.K.; Mahajan, N.N.; Das, S. Fabrication and investigation of influence of $CaCO_3$ as foaming agent on Al-SiCp foam. *Mater. Manuf. Process.* **2019**, *34*, 379–384. [CrossRef]

18. Jain, H.; Gupta, G.; Kumar, R.; Mondal, D.P. Microstructure and compressive deformation behavior of SS foam made through evaporation of urea as space holder. *Mater. Chem. Phys.* **2019**, *223*, 737–744. [CrossRef]

19. Xie, B.; Fan, Y.Z.; Mu, T.Z.; Deng, B. Fabrication and energy absorption properties of titanium foam with $CaCl_2$ as a space holder. *Mater. Sci. Eng. A* **2017**, *708*, 419–423. [CrossRef]

20. Adamek, G.; Jakubowicz, J. Tantalum foam made with sucrose as a space holder. *Int. J. Refract. Met. Hard Mater.* **2015**, *53*, 51–55. [CrossRef]

21. Yang, X.; Hu, Q.; Du, J.; Song, H.; Zou, T.; Sha, J.; He, C.; Zhao, N. Compression fatigue properties of open-cell aluminum foams fabricated by space-holder method. *Int. J. Fatigue* **2019**, *121*, 272–280. [CrossRef]

22. Huang, S.M.; Nauman, E.A.; Stanciu, L.A. Investigation of porosity on mechanical properties, degradation and in-vitro cytotoxicity limit of Fe30Mn using space holder technique. *Mater. Sci. Eng. C* **2019**, *99*, 1048–1057. [CrossRef]

23. Puga, H.; Carneiro, V.H.; Jesus, C.; Pereira, J.; Lopes, V. Influence of particle diameter in mechanical performance of Al expanded clay syntactic foams. *Compos. Struct.* **2018**, *184*, 698–703. [CrossRef]

24. Szyniszewski, S.T.; Smith, B.H.; Hajjar, J.F.; Schafer, B.W.; Arwade, S.R. The mechanical properties and modeling of a sintered hollow sphere steel foam. *Mater. Des.* **2014**, *54*, 1083–1094. [CrossRef]

25. Szlancsik, A.; Katona, B.; Bobor, K.; Májlinger, K.; Orbulov, I.N. Compressive behaviour of aluminium matrix syntactic foams reinforced by iron hollow spheres. *Mater. Des.* **2015**, *83*, 230–237. [CrossRef]

26. Andersen, O.; Göhler, H.; Kostmann, C.; Quadbeck, P.; Diologent, F.; Colas, D.; Kieback, B. Powder metallurgically manufactured cellular metals from carat gold alloys for decorative applications. *Met. Powder Rep.* **2018**, *73*, 72–79. [CrossRef]

27. Ma, Y.; Yang, X.; He, C.; Yang, K.; Xu, J.; Sha, J.; Shi, C.; Li, J.; Zhao, N. Fabrication of in-situ grown carbon nanotubes reinforced aluminum alloy matrix composite foams based on powder metallurgy method. *Mater. Lett.* **2018**, *233*, 351–354. [CrossRef]

28. Kang, K.-J. Wire-woven cellular metals: The present and future. *Prog. Mater. Sci.* **2015**, *69*, 213–307. [CrossRef]

29. Lee, M.-G.; Ko, G.-D.; Song, J.; Kang, K.-J. Compressive characteristics of a wire-woven cellular metal. *Mater. Sci. Eng. A* **2012**, *539*, 185–193. [CrossRef]

30. Hu, J.; Du, Q.; Gao, J.; Kang, J.; Guo, B. Compressive mechanical behavior of multiple wire metal rubber. *Mater. Des.* **2018**, *140*, 231–240. [CrossRef]

31. Osorio-Hernández, J.O.; Suarez, M.A.; Goodall, R.; Lara-Rodriguez, G.A.; Alfonso, I.; Figueroa, I.A. Manufacturing of open-cell Mg foams by replication process and mechanical properties. *Mater. Des.* **2014**, *64*, 136–141. [CrossRef]

32. Matheson, K.E.; Cross, K.K.; Nowell, M.M.; Spear, A.D. A multiscale comparison of stochastic open-cell aluminum foam produced via conventional and additive-manufacturing routes. *Mater. Sci. Eng. A* **2017**, *707*, 181–192. [CrossRef]

33. Feng, X.; Zhang, Z.; Cui, X.; Jin, G.; Zheng, W.; Liu, H. Additive manufactured closed-cell aluminum alloy foams via laser melting deposition process. *Mater. Lett.* **2018**, *233*, 126–129. [CrossRef]

34. Pape, F.; Noelke, C.; Kaierle, S.; Haferkamp, H.; Gesing, T.M. Influence of Foaming Agents on Laser Based Manufacturing of Closed-cell Ti Foam. *Procedia Mater. Sci.* **2014**, *4*, 97–102. [CrossRef]

35. Gao, Q.; Wang, L.; Zhou, Z.; Ma, Z.D.; Wang, C.; Wang, Y. Theoretical, numerical and experimental analysis of three-dimensional double-V honeycomb. *Mater. Des.* **2018**, *139*, 380–391. [CrossRef]

36. Yang, L.; Cormier, D.; West, H.; Harrysson, O.; Knowlson, K. Non-stochastic Ti–6Al–4V foam structures with negative Poisson's ratio. *Mater. Sci. Eng. A* **2012**, *558*, 579–585. [CrossRef]

37. Murr, L.E. Open-cellular metal implant design and fabrication for biomechanical compatibility with bone using electron beam melting. *J. Mech. Behav. Biomed. Mater.* **2017**, *76*, 164–177. [CrossRef]

38. Caiazzo, F.; Campanelli, S.L.; Cardaropoli, F.; Contuzzi, N.; Sergi, V.; Ludovico, A.D. Manufacturing and characterization of similar to foam steel components processed through selective laser melting. *Int. J. Adv. Manuf. Technol.* **2017**, *92*, 2121–2130. [CrossRef]

39. De Pasquale, G.; Luceri, F.; Riccio, M. Experimental Characterization of SLM and EBM Cubic Lattice Structures for Lightweight Applications. *Exp. Mech.* **2019**, 1–14. [CrossRef]
40. Chang, K.; Gao, J.-T.; Wang, Z.; Guo, Z.-C. Manufacturing 3-D open-cell aluminum foam via infiltration casting in a super-gravity field. *J. Mater. Process. Technol.* **2018**, *252*, 705–710. [CrossRef]
41. Bracconi, M.; Ambrosetti, M.; Okafor, O.; Sans, V.; Zhang, X.; Ou, X.; Da Fonte, C.P.; Fan, X.; Maestri, M.; Groppi, G.; et al. Investigation of pressure drop in 3D replicated open-cell foams: Coupling CFD with experimental data on additively manufactured foams. *Chem. Eng. J.* **2018**. [CrossRef]
42. Li, N.; Huang, S.; Zhang, G.; Qin, R.; Liu, W.; Xiong, H.; Shi, G.; Blackburn, J. Progress in additive manufacturing on new materials: A review. *Recent Adv. Addit. Manuf. Met. Alloys* **2019**, *35*, 242–269. [CrossRef]
43. Pokharel, R.; Balogh, L.; Brown, D.W.; Clausen, B.; Gray, G.T.; Livescu, V.; Vogel, S.C.; Takajo, S. Signatures of the unique microstructure of additively manufactured steel observed via diffraction. *Scr. Mater.* **2018**, *155*, 16–20. [CrossRef]
44. Zinovieva, O.; Zinoviev, A.; Ploshikhin, V. Three-dimensional modeling of the microstructure evolution during metal additive manufacturing. *Comput. Mater. Sci.* **2018**, *141*, 207–220. [CrossRef]
45. Gorsse, S.; Hutchinson, C.; Gouné, M.; Banerjee, R. Additive manufacturing of metals: A brief review of the characteristic microstructures and properties of steels, Ti-6Al-4V and high-entropy alloys. *Sci. Technol. Adv. Mater.* **2017**, *18*, 584–610. [CrossRef] [PubMed]
46. Yang, C.; Li, B.; Ren, M.; Fu, H. Micro precision casting based on investment casting for micro structures with high aspect ratio. *Trans. Nonferrous Met. Soc. China* **2009**, *19*, s521–s525. [CrossRef]
47. Dong, X.; Zhu, X.; Ji, S. Effect of super vacuum assisted high pressure die casting on the repeatability of mechanical properties of Al-Si-Mg-Mn die-cast alloys. *J. Mater. Process. Technol.* **2019**, *266*, 105–113. [CrossRef]
48. Yu, W.; Yuan, Z.; Guo, Z.; Xiong, S. Characterization of A390 aluminum alloy produced at different slow shot speeds using vacuum assisted high pressure die casting. *Trans. Nonferrous Met. Soc. China* **2017**, *27*, 2529–2538. [CrossRef]
49. Dong, X.; Yang, H.; Zhu, X.; Ji, S. High strength and ductility aluminium alloy processed by high pressure die casting. *J. Alloys Compd.* **2019**, *773*, 86–96. [CrossRef]
50. Viswanath, A.; Manu, M.V.; Savithri, S.; Pillai, U.T.S. Numerical simulation and experimental validation of free surface flows during low pressure casting process. *J. Mater. Process. Technol.* **2017**, *244*, 320–330. [CrossRef]
51. Sanitas, A.; Bedel, M.; El Mansori, M. Experimental and numerical study of section restriction effects on filling behavior in low-pressure aluminum casting. *J. Mater. Process. Technol.* **2018**, *254*, 124–134. [CrossRef]
52. Snelling, D.; Williams, C.; Druschitz, A. Mechanical and Material Properties of Castings produced via 3d printed molds. *Addit. Manuf.* **2019**, *27*, 199–207. [CrossRef]
53. Shangguan, H.; Kang, J.; Deng, C.; Hu, Y.; Huang, T. 3D-printed shell-truss sand mold for aluminum castings. *J. Mater. Process. Technol.* **2017**, *250*, 247–253. [CrossRef]
54. Upadhyay, M.; Sivarupan, T.; El Mansori, M. 3D printing for rapid sand casting—A review. *J. Manuf. Process.* **2017**, *29*, 211–220. [CrossRef]
55. Sama, S.R.; Badamo, T.; Lynch, P.; Manogharan, G. Novel sprue designs in metal casting via 3D sand-printing. *Addit. Manuf.* **2019**, *25*, 563–578. [CrossRef]
56. Sama, S.R.; Wang, J.; Manogharan, G. Non-conventional mold design for metal casting using 3D sand-printing. *Adv. Manuf. Process. Res.* **2018**, *34*, 765–775. [CrossRef]
57. Xue, Y.; Wang, X.; Wang, W.; Zhong, X.; Han, F. Compressive property of Al-based auxetic lattice structures fabricated by 3-D printing combined with investment casting. *Mater. Sci. Eng. A* **2018**, *722*, 255–262. [CrossRef]
58. Kang, J.; Ma, Q. The role and impact of 3D printing technologies in casting. *China Foundry* **2017**, *14*, 157–168. [CrossRef]
59. Wang, D.; Dong, A.; Zhu, G.; Shu, D.; Sun, J.; Li, F.; Sun, B. Rapid casting of complex impeller based on 3D printing wax pattern and simulation optimization. *Int. J. Adv. Manuf. Technol.* **2019**, *100*, 2629–2635. [CrossRef]
60. Kwon, Y.-D.; Lee, Z.-H. The effect of grain refining and oxide inclusion on the fluidity of Al–4.5Cu–0.6Mn and A356 alloys. *Mater. Sci. Eng. A* **2003**, *360*, 372–376. [CrossRef]

61. Wankhede, D.M.; Narkhede, B.E.; Mahajan, S.K.; Choudhari, C.M. Influence of pouring temperature and external chills on mechanical properties of aluminum silicon alloy castings. *Mater. Today Proc.* **2018**, *5*, 17627–17635. [CrossRef]

62. Eskin, D.G.; Al-Helal, K.; Tzanakis, I. Application of a plate sonotrode to ultrasonic degassing of aluminum melt: Acoustic measurements and feasibility study. *J. Mater. Process. Technol.* **2015**, *222*, 148–154. [CrossRef]

63. Dong, Y.W.; Li, X.L.; Zhao, Q.; Yang, J.; Dao, M. Modeling of shrinkage during investment casting of thin-walled hollow turbine blades. *J. Mater. Process. Technol.* **2017**, *244*, 190–203. [CrossRef]

64. Phetrattanarangsi, T.; Puncreobutr, C.; Khamkongkaeo, A.; Thongchai, C.; Sakkomolsri, B.; Kuimalee, S.; Kidkhunthod, P.; Chanlek, N.; Lohwongwatana, B. The behavior of gypsum-bonded investment in the gold jewelry casting process. *Thermochim. Acta* **2017**, *657*, 144–150. [CrossRef]

65. Bayani, H.; Mirbagheri, S.M.H.; Barzegari, M.; Firoozi, S. Simulation of unconstrained solidification of A356 aluminum alloy on distribution of micro/macro shrinkage. *J. Mater. Res. Technol.* **2014**, *3*, 55–70. [CrossRef]

66. Kumar Nayak, R.; Venugopal, S. Prediction of shrinkage allowance for tool design of aluminium alloy (A356) investment casting. *Mater. Today Proc.* **2018**, *5*, 24997–25005. [CrossRef]